Dielectric Flow- and Tab-Based Battery Thermal Management System For EV High Performance Application

Eneko Gonzalez-Agirre[a,c,*], Jon Gastelurrutia[a], Laura Oca[b], Luis del Portillo-Valdes[c], Leire Erbiti Goienetxe[a]

[a]IKERLAN Technology Research Centre, Basque Research and Technology Alliance (BRTA), P.° J.M. Arizmendiarrieta, 2, Arrasate/Mondragón, 20500, Spain
[b]Mondragon Unibertsitatea, Electronic and Computer Science Department, Loramendi 4, 20500 Mondragon, Basque Country, Spain,
[c]Energy Engineering Department, University of the Basque Country (UPV/EHU), Engineering School of Bilbao,

Abstract

From the perspectives of security, durability, and proper operation, effective temperature control via thermal management systems (TMSs) on lithium-ion batteries is crucial for electric vehicle use. In this regard, a novel TMS based on dielectric flow and tab cooling was presented in this paper. A functional prototype of the system was developed and experimentally tested for performance analysis. A thermal model was built on computational fluid dynamics software, and a comparative analysis of the initial and an optimised geometry of the prototype was carried on after validation. Results demonstrate the adequate response of the system. Thermally speaking, temperature decrease was noticed during operation, and the internal and among-cells thermal gradient was preserved into the recommended span. Besides, the used dielectric fluid assisted with a low auxiliary consumption due to its particular viscosity. With the new geometry, the dielectric flow duct volume was reduced by 79.8%, and the system particularities were enhanced due to heat dissipation improvement: operating temperatures were even lower in every scenario examined. The temperature difference among cells was reduced by 15%. Thermal dispersion within the cells was still below the limit, despite being increased. Moreover, the necessary pumping energy consumption was below 0.004% of the exchanged battery module's energy, demonstrating the TMS efficiency. Thus, the application potential of the dielectric tab cooling-based system for electric vehicles was highlighted.

Keywords: Thermal management system, dielectric flow, tab cooling, electric vehicle, lithium-ion battery, electromobility

1. Introduction

Electrification of goods and people transport represents a crucial pace toward decarbonising our society, accounting for around 27% of global CO_2 emissions [1]. On the path to replacing the prevailing internal combustion engine vehicles, battery electric vehicles (BEVs) are put forward as the main alternative, ahead of less energy-efficient mobility technologies such as hydrogen-based fuel cell electric vehicles or even synthetic hydrocarbons, prevailing well-to-wheel efficiency [2, 3].

BEV's expansion relays on the Lithium-ion Battery (LIB) energy storage system, which has been broadly employed in consumer electronics over the last years. This mature technology stands out because of its good energy density, significant power storage capacity, lack of memory effect and high efficiency ratios of 90%-98% [4, 5]. However, these batteries' main downside stands in their great overheating potential, critically exacerbated by the high demanding performances and fast charging. Durability and performance are entirely associated with working temperature and its gradients inside and between cells. This operational temperature span encompasses between -20 °C and 60 °C, with the optimal range around 20 °C - 40 °C and the maximum temperature dispersion of 5 °C. Additionally, high C-rates accelerate degradation, deteriorating battery capacity and power capabilities [6–12].

Proper operation and major security are essential to counter this degradation and ensure a longer life span. Therefore, thermal stress is controlled through battery

---

[*] Corresponding author: IKERLAN Technology Research Centre, Basque Research and Technology Alliance (BRTA), P.° J.M. Arizmendiarrieta, 2. 20500 Arrasate/Mondragón, Spain

Email address: `eneko.gonzalez@ikerlan.es` (Eneko Gonzalez-Agirre)

TMSs. These systems are in charge of temperature adaption inside the optimal range of operation, using different approaches. Air cooling was used at the beginning of commercial BEVs, being an easily implementable and economic system. However, the necessary cooling contact area, due to low thermal conductivity and specific heat capacity properties of air, decreases the battery pack (BP) energy density and makes it unsuitable for high-current charge and discharges. Moreover, air type TMS auxiliary consumption increases broadly in the attempt for proper cooling of battery cells in comparison with other technologies such as liquid TMS [13–16].

This liquid TMS has been the predominant substitute of the air type method, through cold plates (CPs) use. It is an effective system capable of reducing cell temperature below the optimal working point even under demanding applications and LIBs abuse conditions. Nevertheless, there is always a thermal resistance between the battery and the heat transfer fluid due to the need for electrical insulation, reducing the overall heat transfer capacity. Moreover, the system's weight, cost and auxiliary energy consumption are also incremented [17–19].

The phase change material (PCM) solution has also been deeply studied in the past few years. This passive technology uses phase changing effect to absorb the thermal energy by latent heat, which avoids temperature change on the TMS device. Paraffin wax is usually the employed element, having a melting/solidification process. However, the low thermal conductivity of the material obliges it to be incorporated into a porous aluminium structure to increase the heat transfer of the device [20, 21]. The PCM has a high heat absorption capacity avoiding abrupt temperature increases or heat power peaks, so it is particularly indicated as a thermal security element [22]. Even so, an active auxiliary system for solidification and thermal characteristics recovery is needed, losing the main benefits of the system [23, 24].

Recently, the use of dielectric liquids for battery thermal management systems (BTMSs) has gained interest in the research community. These systems are the natural evolution of air and coldplate systems, bringing together the benefits of both systems. The first one uses the least expensive dielectric fluid, which improves the system's simplicity. In contrast, the latter's ability to regulate heat is increased when liquid is used instead of air. These dielectric fluids enable direct contact cooling between the battery cells and the coolant, enhancing heat transfer. Moreover, disposal of intermediary elements such as the coldplates, can reduce energy density and specific energy ratios of the BP.

These systems approach is usually fully immersing the batteries into the dielectric fluid, being capable of reducing the cell maximum temperature compared with the most extended coldplate TMS [25–27]. This temperature reduction is especially effective under high C-rates, where higher heat dissipation capability is required [28]. Moreover, these system usages can provide lower pressure drop and therefore reduced parasitic power consumption [26, 28]. In this way, the battery module (BM) geometry has a significant effect on the temperature of the cells; by reducing the space between cells, the maximum temperature can be reduced due to the velocity increase of coolant fluid, which at the same time increases the pressure drop of the system [15]. All these literature publications have worked under fully immersion concepts for their TMS approaches. Cells could be partially immersed and obtain reasonable temperatures for the BM [29]. Something similar happens with tab or radial cooling configurations. Radial cooling causes a faster temperature drop, whereas tab cooling reduces the internal thermal gradient of the cell [30]. This point is important as the thermal management results will differ depending on the approach of the TMS selected, and if partial or full dielectric immersion, surface cooling or tab cooling is chosen. In this regard, several studies have analysed the degradation and performance effect tab cooling has on the cells.

Hunt et al. [31] studied the degradation process between tab and surface cooling for pouch cells, demonstrating the importance of the thermal gradient nature. A higher cell capacity decrease was noticed when the thermal gradient was perpendicular to cell layers (surface cooling), creating uneven performance and ageing. In contrast, the thermal gradient along cell layers (tab cooling) allows uniform distribution of degradation and better performance.

Dondelewski et al. [32] continued comparing both cooling approaches, concluding that surface cooling results in lower usable capacity and energy than tab cooling. However, analysing the cell geometry effect on the cooling configuration determined that tab cooling is not always better in degradation terms, as a lower cell performs better than a longer cell in terms of heat dissipation when it comes to tab cooling [33]. In that regard, increasing the heat-releasing ability (i.e. improving the conductivity through the tab) will make the difference, as analysed by Li et al. [34], showing the importance of the tab and current collector design for proper heat release and internal temperature homogenisation. Tab cooling can therefore gain in importance with new 'tabless' cell designs proposed, reducing the electrical and thermal resistance caused by the current collector on today's cylindrical cells [35], and be highly beneficial for the TMS.

Deduced from the literature cases explained, both tab cooling and dielectric TMS approaches show possibilities of great benefit for the BEV system, influencing the security and efficiency of the battery pack, as well as improving its energy density and specific energy.

This work implements both outstanding ideas in the previous lines of this paper. For this purpose, a dielectric fluid TMS was developed under tab cooling configuration. By this, dielectric cooling flow is implemented on both tabs of a battery module formed with twelve cylindrical cells, behind the idea of studying the benefits and implementation possibilities of the technology. The results will be primordial and could help in the future design of these systems to increase energy density and specific energy ratios when reducing the necessary space on the BP for the TMS or even reducing the necessary coolant quantity, as well as reducing the auxiliary energy consumption while maintaining similar thermal management ability. This will make the system more efficient compared with classical cold plate systems or with standard complete dielectric immersion solutions, which make use of all the battery cell surfaces for a higher heat dissipation capacity, whereas tab cooling focuses on the tab area for a more compressed solution.

Followed methodology in the work considers a battery module, where tab cooling can be implemented to avoid any leakages. In that regard, a prototype was constructed, and the thermal model was developed and validated with experimental results. Then an analysis of the TMS system was carried out to optimise the system's heat transfer capacity.

Therefore, the main objective of the work is to search for the feasibility of this technology and how an industrial-level design should be for real implementation. It will improve the published works in energy density and specific energy while allowing performance under fast charge and demanding driving.

2. Battery module and dielectric thermal management system description

The dielectric tab cooling prototype is made of a polyethylene machined structure, where the cells are introduced and encapsulated, forming the necessary duct on cells' tabs for the dielectric fluid to flow through. These duct dimensions are 262.5 x 69.5 x 22.5 mm, and are sealed with a rubber pad between the structure and the transparent cover. All sensor connections are added at both sides, with three thermocouples (top, middle body and bottom) for temperature measurements and voltage readings on every cell tab. The prototype geometry can be seen in fig. 1.

Table 1: Properties of LithiumWerks ANR26650m1B cell [36].

LithiumWerks ANR26650m1B	
Chemistry	LFP
V_{nom} [V]	3.3
Cap_{nom} [Ah]	2.5
Max CHA Current [A]	10 (4C)
Max DCH Current [A]	50 (20C)
Temperature Range [°C]	0 to 55
Diameter [mm]	26
Length [mm]	65
Mass [kg]	0.076

Electrically speaking, the module comprises 12 LithiumWerks ANR26650m1B cylindrical LFP cells with 2.5Ah capacity each. The table 1 shows cell's specification. Cells are connected in 12S1P configuration, obtaining 39.6 V and 2.5Ah module.

Following the BP requirements previously stated for a combustion vehicle's electrification case study [37], a theoretical extrapolation from the battery module to the battery pack level was done. Thus, establishing the battery cycling C-rate and the appropriate dielectric volumetric flow rate. An amount of 290 prototype modules should be needed on a 10S29P configuration to assemble a 28.71kWh and 72.5Ah battery pack. Consid-

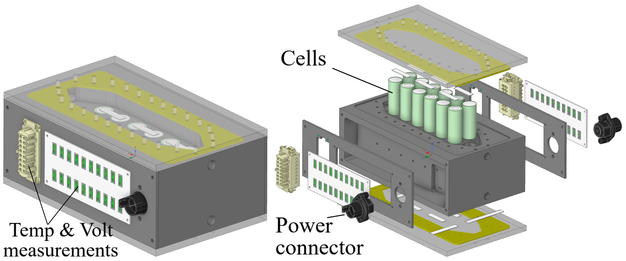

(a) Complete geometry. (b) Exploded geometry.

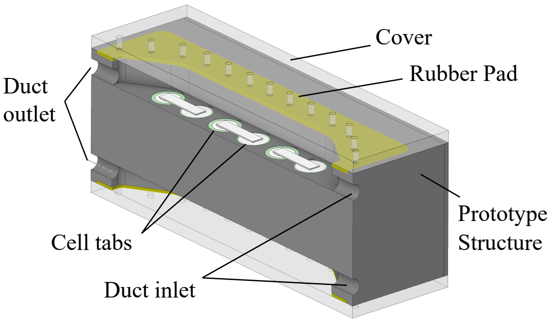

(c) Cross section.

Figure 1: Dielectric tab cooling TMS geometry.

ering the theoretical battery pack's electrical configuration and the constant driving energy consumption of the vehicle at 120km/h [38], the electrical profile to be used was defined. Hence, each cell's discharging current was estimated at 3.45A, corresponding to a 1.38C-rate. On the other hand, the charge was carried out to the cell's maximum capability, performing a fast charge of 4C. The selected working span was specified between 10% and 90% of the state of charge (SOC).

The dielectric fluid used for cooling was the hydrofluoroether (HFE) 7200, with a boiling point of 76 °C, zero ozone depletion and low global warming potential. It also has a low viscosity, which is of great importance in reducing auxiliary energy consumption. This also eases achieving a turbulent flow, increasing the heat transfer capacity. The fluid properties are shown in table 2.

Table 2: HFE 7200 fluid thermophysical properties. [39–42]

T [°C]	ρ [kg m^{-3}]	**C**$_p$ [J kg^{-1} °C^{-1}]	k [W m^{-1} °C^{-1}]	ν [m^2 s^{-1}]	μ [Pa s]
-30	1550.2	1148.6	8.48e^{-2}	8.76e^{-7}	1.36e^{-3}
-20	1527.2	1192.5	8.05e^{-2}	7.39e^{-7}	1.13e^{-3}
-10	1504.1	1236.3	7.66e^{-2}	6.28e^{-7}	9.44e^{-4}
0	1481.1	1280.2	7.30e^{-2}	5.45e^{-7}	8.08e^{-4}
10	1458.1	1324.1	6.97e^{-2}	4.73e^{-7}	6.90e^{-4}
20	1435.0	1367.9	6.67e^{-2}	4.19e^{-7}	6.02e^{-4}
30	1412.0	1411.8	6.41e^{-2}	3.78e^{-7}	5.34e^{-4}
40	1389.0	1455.7	6.17e^{-2}	3.42e^{-7}	4.76e^{-4}
50	1366.0	1499.5	5.97e^{-2}	3.15e^{-7}	4.31e^{-4}

Regarding the dielectric flow rate used, the hydraulic connection between modules was studied. BP's maximum dielectric flow rate was 20 l/min [38]. That flow rate was divided into cooling loops, formed by the 290 modules divided into serialised groups of 10, 29 or 58 modules. This gives a flow for each module of 0.7 l/min, 2.0 l/min and 4.0 l/min.

3. Battery and TMS models

This section explains the models and their use for the consequent analysis. A lumped thermal model for heat generation of the cells was used, co-simulating it through the primary 3D CFD model for the BTMS analysis.

3.1. Co-simulation between CFD model and cell heat generation FMU

The co-simulation process between the heat generation lumped thermal model and the CFD thermofluidics model was performed by the Functional Mock-Up Interface (FMI) standard, which allows the exchange of dynamic simulation models. With that aim, the thermal lumped model was exported as a Functional Mock-Up Unit (FMU), which can be read by the CFD software, where both models were co-simulated. In that process, cell temperature from computational fluid dynamics (CFD) feeds the FMU, whereas the generated volumetric heat on each cell is transferred from the lumped model to the CFD. Model interaction and the lumped thermal model scheme are explained in fig. 2.

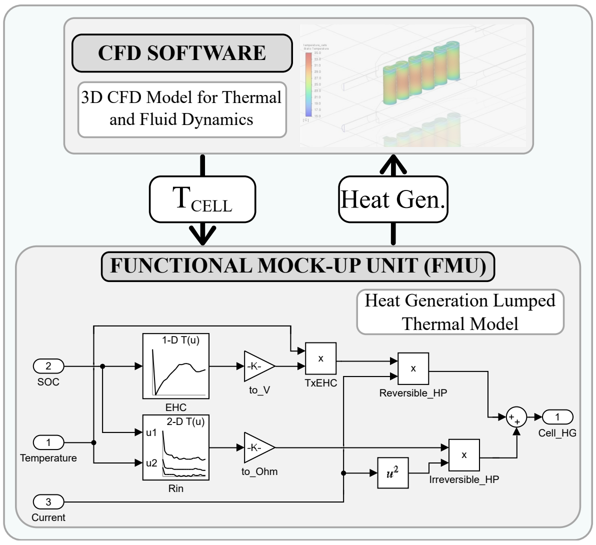

Figure 2: Co-simulation scheme between models.

3.2. Lumped heat generation thermal model

The lumped heat generation model was developed following the eq. (1), where Bernardi et al. [43], defined the reversible and irreversible heat generation effects of cells. As was previously emphasised, considering both effects on the cell's characterisation is essential for adequate thermal behaviour analysis [37].

$$\dot{Q} = I^2 \cdot R_{in} + I \cdot T \cdot \frac{dU^{avg}}{dT} \tag{1}$$

I [A] is the cell charging (positive) or discharging (negative) current, R$_{in}$ [Ω] is the internal resistance of the cell, T [K] is the cell's temperature, and $dU^{avg} \cdot dT^{-1}$ [V·K^{-1}] is the entropic heat coefficient (EHC) defined by equilibrium potential changes to temperature. Both

Table 3: CFD model element properties.

	Material	Dimensions (x, y, z) [mm]	ρ [kg m^{-3}]	C$_p$ [J kg^{-1} °C^{-1}]	k [W m^{-1} °C^{-1}]
Cell	-	∅=26, l=65	2318.14	1089.6	axial= 2.17, radial=0.434
Busbar	Steel	40 x 13 x 0.6	8030	502.48	16.27
Structure	PE1000	312.5 x 51.75 x 130.15	930	1800	0.4

thermal parameters of the cells were experimentally characterised. The internal resistance (R$_{in}$) values were measured through the Hybrid Power Pulse Characterisation (HPPC) tests [44], with constant current charge and discharge pulses of 18 seconds for three temperature levels all over the SOC scope. Moreover, EHC measurements were carried on by variable temperature potentiometry [45]. Both measured parameters can be seen in fig. 3.

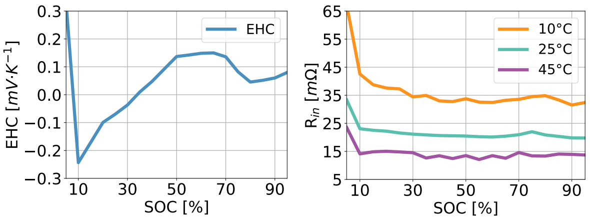

(a) Entropic Heat Coeficient.

(b) Internal Resistance.

Figure 3: ANR26650m1B cell's properties for heat generation model.

The lumped heat generation model estimates each cell's variable heat production, which only depends on the instantaneous electrical solicitations in the form of current. The current is employed to evaluate the instantaneous SOC value using the Coulomb Counting approach, and a volume-averaged temperature is calculated (from CFD) at each cell every time step. With those two last values, the entropic heat coefficient and the internal resistance are calculated at every time step. These determine the entropic and ohmic heat, resulting in the cell's total heat generation for that time step, as represented in fig. 2.

3.3. 3D CFD model

With the lumped model generated, the CFD model was developed. Intending to reduce the computational cost, the prototype's constructive particularities were simplified but still provided a realistic idea of the thermal distribution inside the module. Moreover, only half of the BM explained in section 2 was included in the computational domain, incorporating a symmetry plane. Therefore, six cells with their respective busbars and half of the two top and bottom ducts for the dielectric flow were included, as seen in fig. 4.

The battery cells were treated as homogeneous volumes, as the lumped thermal model replaces the heat generation associated with the processes dependent on the internal geometry construction of the cell. Nevertheless, cylindrical-orthotropic thermal conductivity was used, defining the radial and axial thermal conductivity values experimentally obtained from the hot disk transient plane source technique [46]. Uniform thermal capacity was also used, acquired from experimental measurements by means of accelerating rate calorimetry (THT, EV Standard Calorimeter) [47]. Materials and properties were defined following the data in table 3.

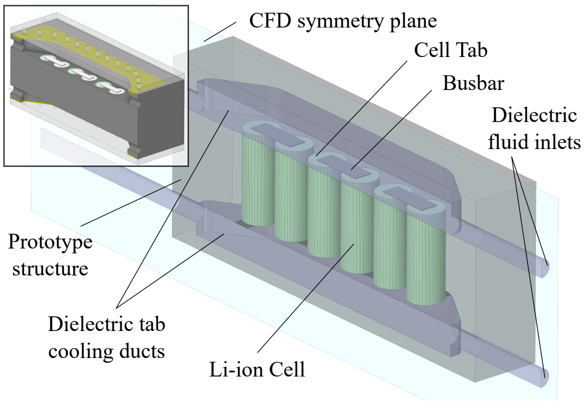

Figure 4: Geometry for the CFD model of the BTMS.

The Navier-Stokes (RANS) equations' Reynolds Average method and the Energy equation on [48] were employed to incorporate turbulence effects into the fluid region's mean flow variables. In order to achieve an accurate description of the hydrodynamic and convective heat transfer phenomena, the flow regime, which was considered turbulent in the velocity range examined, was modelled using the Realizable k-epsilon viscous model [49] and a two-layer near wall treatment [50]. Mass-flow inlet and pressure outlet were defined as fluid boundary conditions, so different cooling capacities can be simulated. Heat generation in the busbars by joule heating is also contemplated, introducing the current density through the material.

To ensure the model results are independent of the mesh used during the CFD analysis, a grid refinement study was done for the geometry, focusing on the fluid. The procedure followed is the Grid Convergence Index (GCI) analysis, based on the Richardson Extrapolation method [51]. Thereby, three different meshes were created, and the discretisation error when comparing the results for the pressure drop and the heat transfer coefficient on the dielectric fluid duct was compared. Results can be seen in fig. 5, for the coarse mesh (N_1: 1,099,821 elements), the medium mesh (N_2: 2,231,507 elements) and the fine mesh (N_3: 9,135,272 elements) with a resulting refinement factor of $r_{21} = 1.26$ and $r_{32} = 1.6$. Both GCI factors were nearly zero for the pressure drop results and heat transfer coefficient. The relative error between meshes for pressure drop was $e_{relative21} = 4.22\%$ and $e_{relative32} = 0.25\%$ and for the heat transfer coefficient $e_{relative21} = 2.62\%$ and $e_{relative32} = 0.82\%$. These results show a clear convergence tendency with mesh refinement. Therefore, the medium N_2 mesh was selected owing to mesh elements and results concordance.

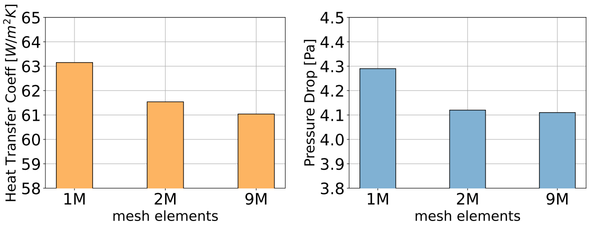

(a) Heat transfer coefficient results.

(b) Pressure drop results.

Figure 5: Grid refinement study results.

4. Experimental analysis and results

This section covers the experimental tests carried out to analyse the dielectric tab cooling TMS's properties. Following, the CFD model was validated through experimental data.

4.1. Experimental test setup

An experimental setup was developed to study the TMS's thermal performance all over the system's operational scope.

The hydraulic circuit of the TMS was formed with two independent loops; the first and main one comprehended the prototype's ducts with an independent pump for the dielectric fluid and was thermally connected to the second one by a coil heat exchanger. This latter loop employed the water of a chiller to control the dielectric fluid's temperature on the main loop. The scheme of this configuration can be seen in fig. 6a.

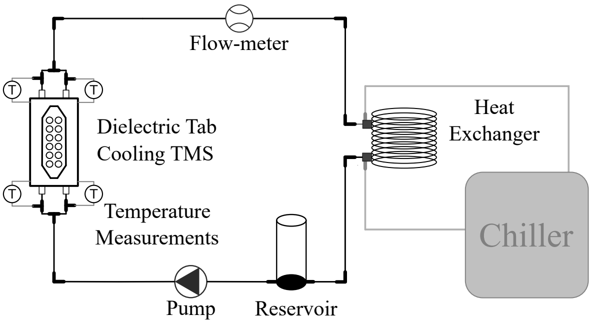

(a) Experimental setup scheme.

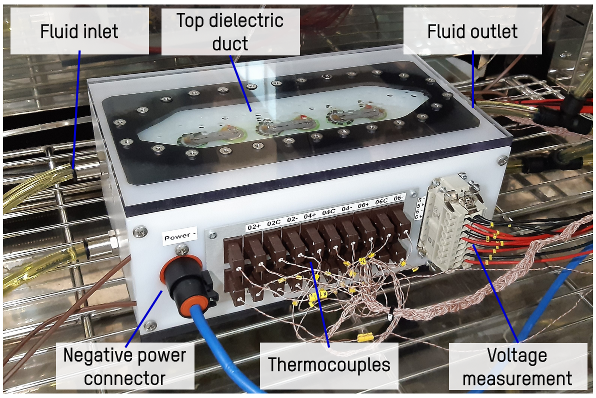

(b) Dielectric tab cooling TMS.

Figure 6: TMS experimental tests.

The electrical profile used on the tests, as explained in section 2, was a cycle of 1.38C discharge followed by a 4C fast charge, with the SOC range oscillating between 90% and 10% continuously. To carry out such tests, the battery was connected to a programmable cycler (Industrial Battery Tester (IBT) with ± 0.1% accuracy of full scale, which runs with Digatron Firing Circuits BTS-600 software for data evaluation). This cycle was repeated six times for the prototype temperature to stabilise, so the thermal jump from the initial to the final temperature could be checked. The ambient temperature was adjusted to the inlet temperature of the dielectric fluid by testing it in a thermal chamber (CTS, Clima Temperatur Systeme) with an accuracy of ±0.3K and a temperature range from -70 °C to +180 °C.

Cells' temperature was measured on the positive tab, negative tab and body surface using an Agilent 34970A data acquisition system and T-type thermocouples. Moreover, each cell's voltage was also measured for module security and stabilisation purposes. As seen in fig. 6b, these connections were made on the prototype side faces. The accuracy specifications of the Agilent are ±0.0035% of reading and 0.0005% of range for voltage. Moreover, the temperature accuracy of Agilent is ±0.5 °C of range and 0.2% of reading and the type-T thermocouple has ±1.0 °C tolerance.

4.2. *Experimental test results*

The experimental test results were divided into two blocks. The first block refers to the volumetric flow rate change study, whereas fluid inlet temperature was changed in the second part. Therefore, three tests were accomplished in the first block at 25 °C with the volumetric flow rate at 0.0 l/min, 0.7 l/min and 3.2 l/min, being the last the maximum flow rate achievable with the used pump. In the second part of the study, three more tests were done at 0.7 l/min, with the fluid inlet temperature at 15 °C, 25 °C and 35 °C, respectively.

The temperature evolution of cells during the tests was analysed. The average temperature during the module cycling is shown in fig. 7a for the flow change tests and in fig. 8a for temperature change tests. Moreover, a coloured band is also shown, enclosing each test's maximum and minimum cell temperatures.

On the other hand, fig. 7b and fig. 8b showed the thermal jump of each test (ΔT_{test}). This value was calculated by the difference from the initial test temperature to the averaged temperature of the last cycle, once the module temperature between test cycles was stabilised.

All of the tests showed quick stabilisation time due in a certain way to the cells' relatively low heat generation and the system's effective cooling capacity. The case without fluid flow in fig. 7a illustrates this, where

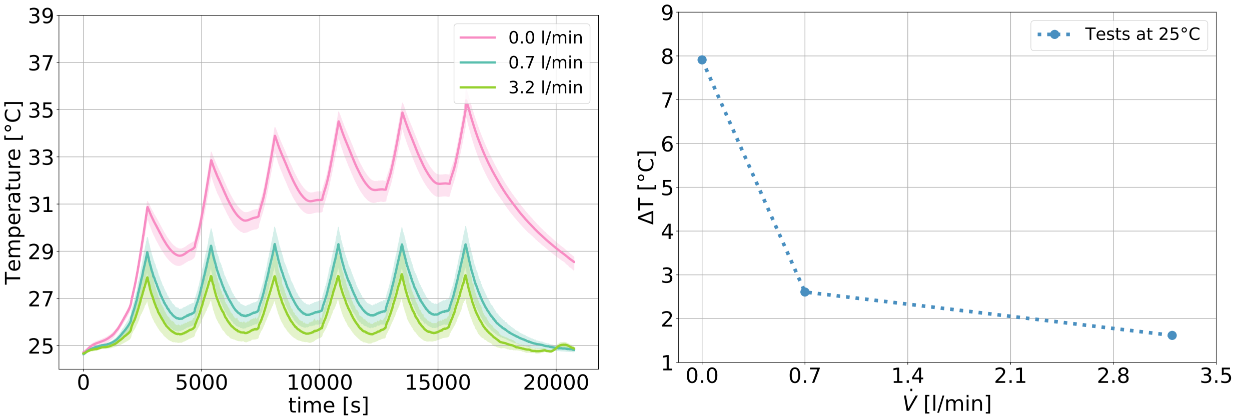

(a) Volumetric flow rate change under experimental cycle.

(b) Thermal jump of the stabilised experimental cycle with respect to the initial temperature, under volumetric flow rate change.

Figure 7: Volumetric flow rate change results for 25 °C inlet temperature condition.

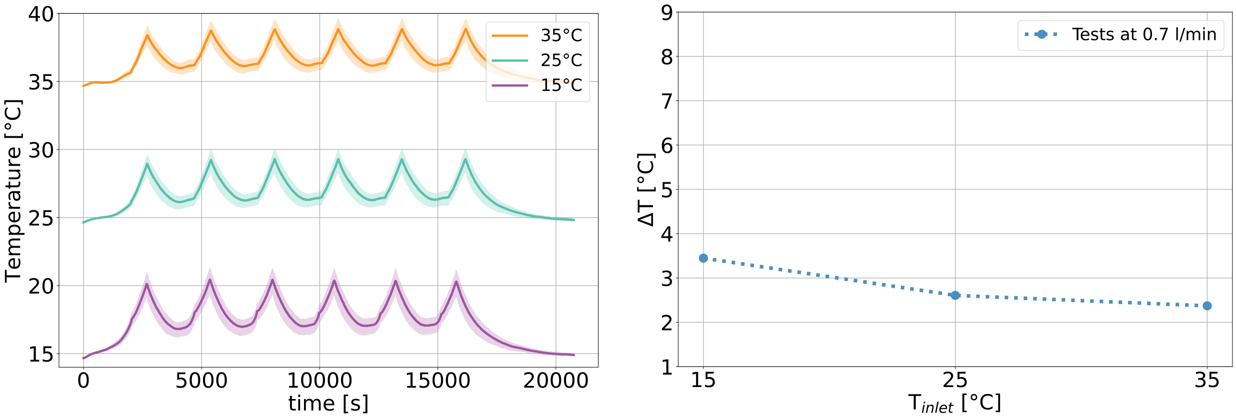

(a) Fluid inlet temperature change under experimental cycle.

(b) Tests' thermal jump (ΔT_{test}) from the initial temperature to the last cycle averaged temperature, under fluid inlet temperature change.

Figure 8: Fluid inlet temperature change results for 0.7 l/min volumetric flow rate condition.

after the six electric cycles, the ΔT_{test} increase was 7.9 °C, considerably higher than all of the rest of the tests, and the temperatures seem to be increasing (no stabilisation). Regarding the other two tests in fig. 7, the ΔT_{test} was reduced from 2.6 °C to 1.6 °C as the volumetric flow rate increased from 0.7 l/min to 3.2 l/min.

Concerning results on the inlet temperature changing tests, the ΔT_{test} reduction as inlet temperature was increased can be seen in fig. 8b. This effect is predominantly due to the cell heat generation change over the temperature scope. The cell's internal resistance is considerably increased at low temperatures, as shown in fig. 3b. Therefore, the heat generation due to the irreversible effect is higher than at more elevated temperatures. At the test scope between 15 °C and 35 °C, the heat generation reduction entails a ΔT_{test} reduction from 3.4 °C to 2.3 °C.

The temperature dispersion among cells on the module (ΔT_{module}) was also compared, as seen in table 4. The maximum ΔT_{module} was identified at 15 °C and 2.0 l/min test, with a value of 2.7 °C. A similar effect can be found concerning the maximum temperature dispersion inside each cell (ΔT_{cell}), with a 2.7 °C value localised on the same test. This effect is due to the combination of high cells' heat generation at low operating temperatures and the high flow rate, which results in elevated heat dissipation difference from one cell to another. Referring to the lowest ΔT_{module} and ΔT_{cell}, 1.2 °C and 0.9 °C were identified respectively on the 0.0 l/min and 25 °C test. In every test, the thermal dispersion was kept below the recommended 5 °C.

These results demonstrated the need to work at mid-high temperatures to reduce the cells' heat generation. There is also no need for high volumetric flow rates for dielectric tab cooling TMS efficient working.

Table 4: Experimental results: Test ending temperature averaged on the last cycle ($T_{avg\ last-cycle}$), thermal jump of the test (ΔT_{test}), and maximum thermal dispersion among cells on the module (ΔT_{module}) and inside cells (ΔT_{cell}).

Test	$\mathbf{T}_{avg\ last-cycle}$ [°C]	$\mathbf{\Delta T}_{test}$ [°C]	$\mathbf{\Delta T}_{module}$ [°C]	$\mathbf{\Delta T}_{cell}$ [°C]
15 °C - 0.7 l/min	18.1	3.4	2.0	2.4
15 °C - 2.0 l/min	17.0	2.5	2.7	2.7
25 °C - 0.0 l/min	32.6	7.9	1.2	0.9
25 °C - 0.7 l/min	27.2	2.6	1.8	2.0
25 °C - 3.2 l/min	26.3	1.6	2.2	2.4
35 °C - 0.7 l/min	37.1	2.4	1.6	1.6
35 °C - 2.0 l/min	36.1	1.7	1.9	1.9

4.3. Model validation results

From the experimental tests previously presented, three were selected to perform the validation process of the dielectric TMS CFD model. 15 °C and 35 °C tests at 0.7 l/min were selected to check the model's response to temperature change, whereas the test at 25 °C at 3.2 l/min was used to verify the flow rate change effect. The six cycles, as in the experimental tests, were replicated with the model to validate the whole thermal performance observed on the prototype.

The validation results for the three studied cases can be seen in fig. 9 with the experimental (continuous line) and numerical (discontinuous line) temperature evolution. The absolute error (e_{abs} [°C]) is placed below them, showing the difference between the experimental and CFD temperature values. Thus, the maximum error was 1.92 °C, whereas the mean errors were 0.88 °C, 0.39 °C and 0.34 °C for the 15 °C, 25 °C and 35 °C cases, respectively.

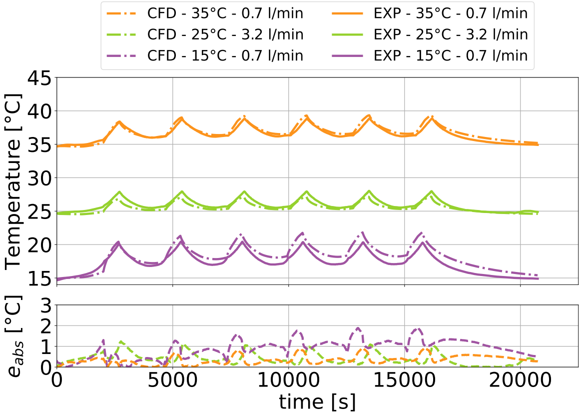

Figure 9: Model validation results: temperature evolution of the experimental tests (continuous line) and numerical tests (discontinuous line), and the absolute error (e_{abs}) between them.

The results show that the dielectric TMS model correctly follows the heat generation and transfer phenomena on the analysed cycles. It properly captures the charging and discharging processes and the associated physical effects on the battery temperature. In addition, it accurately represents the various ΔT_{test} over the different test conditions. Therefore, the battery module and the thermal management system were adequately characterised, and the CFD model can be employed in the following analysis.

5. Dielectric TMS duct optimisation and analysis results

This section focuses on the CFD analysis of the dielectric prototype. Initially, the duct size changing possibility was studied for the TMS optimisation. This was performed after observing the flow's laminarity due to the prototype's excessive duct size. With its reduction, the flow turbulence could be increased and heat transfer capacity enhanced. Therefore, the optimal duct size was looked for. With the resultant optimised geometry, the calibrated model was used to perform a CFD study on the duct change to enhance the heat dissipation capacity and the energy density of the dielectric tab cooling system.

5.1. *TMS duct optimisation*

For the duct optimisation process, a simplified lumped thermal model was used. This model represents the prototype's heat generation and dissipation process, calculating the maximum cell temperature under thermal equilibrium when both heat generation and dissipation are stabilised, computing the heat transfer coefficient to the dielectric fluid and, thus, the thermal resistance on the duct surface.

The duct was divided into two narrower channels, so each of them passes through the tabs of one cell row. The estimation was done under the three different volumetric flow rates each battery module would have under different hydraulic connections, as mentioned in section 2; 0.7 l/min, 2.0 l/min and 4.0 l/min. Moreover, two duct heights, 5 mm and 10 mm and four widths of 10 mm, 15 mm, 20 mm and 26 mm were studied, being the last width the same dimension as the cell diameter.

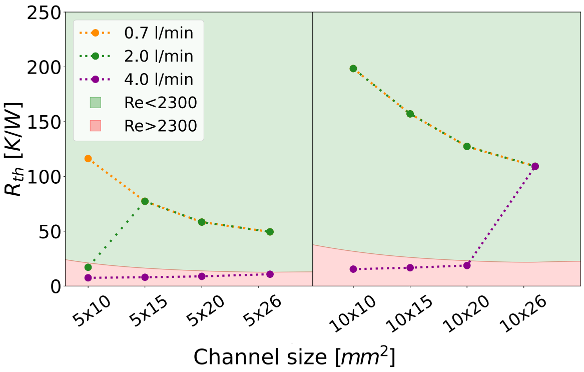

Figure 10: Duct size optimisation analysis.

The results in fig. 10 also show the Reynolds number value of the flow, being the green-coloured top zone laminar flow zone and the red area below the turbulent zone. As can be seen, with high flow rates, the flow becomes turbulent, and the thermal resistance reduces drastically as the heat transfer is enhanced. When the volumetric flow rate is not high enough to reach the turbulent zone, the thermal resistance is reduced as duct width reaches cell diameter size. Both flows on the laminar zone (0.7 l/min and 2.0 l/min) show little difference due to the correlations on that regimen being mainly duct size and not flow speed dependant.

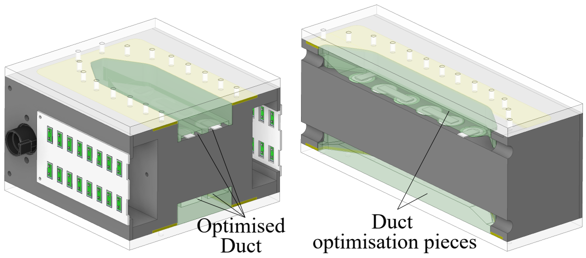

(a) Widthwise view of Geom02 design. (b) Lengthwise view of Geom02 design.

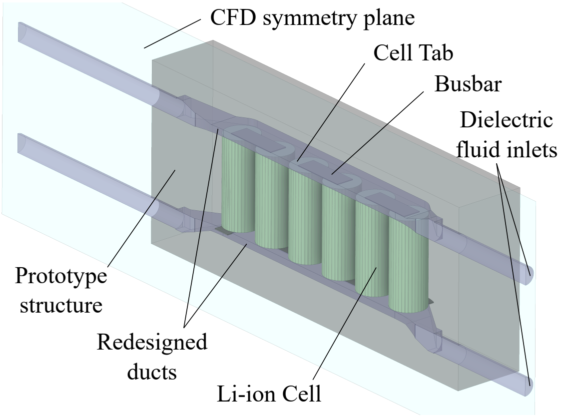

(c) CFD model geometry.

Figure 11: Enhanced duct geometry *Geom02*.

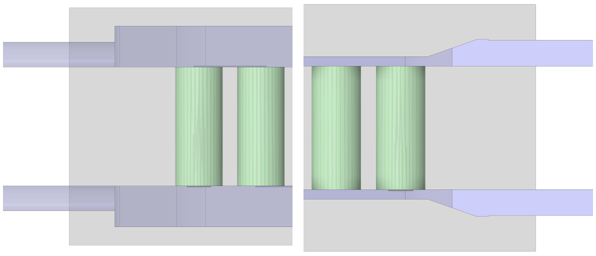

Figure 12: Front view comparison between *Geom01* (left) and *Geom02* (right).

Therefore, considering that different hydraulic connections or flow rates could be used, 5 mm x 26 mm was chosen as the most appropriate duct size to enhance the heat transfer. The duct must cover the entire cell tab to increase the heat transfer area, and having a 5 mm height helps flow to increase its turbulence. The resultant geometry, hereafter called *Geom02*, is designed by inserting an extra polyethene machined piece on the duct for flow canalising as can be seen in fig. 11a and fig. 11b and also compared in fig. 12. This modular design facilitates experimentally testing diverse duct shapes and sizes. Moreover, fig. 11c shows the consequent CFD model's simplified geometry.

With the new geometry, GCI was conducted once again to verify the results' independence from the geometry change. The three meshes employed in the study (N_1: 2,037,014; N_2: 4,114,147; N_3: 16,115,061) had a refinement factor of r_{21}=1.26 and r_{32}=1.57, and the pressure drop and heat transfer coefficient were measured as seen in fig. 13. The GCI factor for heat transfer coefficient was nearly zero, whereas for the pressure drop low values of $GCI_{21\_\Delta p}$=0.46% and $GCI_{32\_\Delta p}$=0.17% were achieved. With this convergence tendency results, the medium N_2 mesh was selected for the following simulations.

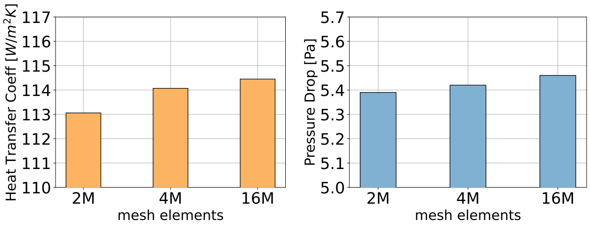

(a) Heat transfer coefficient results.

(b) Pressure drop results.

Figure 13: Grid refinement study results.

5.2. *Enhanced TMS CFD analysis and results*

Several cases were simulated using CFD to compare the dielectric TMS with the initial geometry, referred to as *Geom01*, and duct-improved *Geom02*. In that regard, experimental tests' charging and discharging conditions were kept on while reducing the cycle number. Hence, only one cycle formed by a 4C charge followed by a 1.38C discharge was simulated for every case.

In this analysis, four of the experimental test conditions were replicated. Three of them used 0.7 l/min volumetric flow rate at 15 °C, 25 °C and 35 °C for temperature change effect evaluation. Moreover, a case at 4.0 l/min and 25 °C was utilised to study the flow rate changing effect. With the resultant data, both geometries were compared from the thermal and hydraulic points of view. Cell temperature evolution for *Geom01* and *Geom02* can be seen in fig. 14. Moreover, diverse simulation results are shown in table 5.

The maximum temperature of the cycle (T_{max}) and the maximum thermal gradient among cells in the battery module (ΔT_{module}) can be seen, followed by the maximum thermal gradient inside the cells (ΔT_{cell}). Furthermore, the fluid pressure drop (Δp [Pa]) on the duct was used for auxiliary consumption estimation, calculating the resultant dielectric fluid pumping energy consumption (E_h [Wh]). This was evaluated following eq. (2), where the power consumption corresponding to the pressure drop and volumetric flow rate ($\dot{v}$ [m^3/s]) relation was interpolated on the cycle time span ($t_0 - t$).

$$E_h = \int_{t_0}^{t} \left(\dot{V} \cdot \Delta p\right) dt \tag{2}$$

For every case studied, the temperature all over the cycle was lower with *Geom02*, reducing the maximum temperature from 1.4 °C to 0.7 °C, depending on the case. Besides, the case with the highest ΔT_{module} was also reduced from 2 °C to 1.7 °C, whereas the ΔT_{cell} was increased from 2.7 °C to 3.7 °C. This is a direct consequence of the increased heat transfer capacity after the duct geometry change. The four cases analysed showed the same tendency as the experimental results data in section 4.2; at higher temperatures, the thermal jump (ΔT_{test}) decreases, the same as with high volumetric flows. All these data can be summarised in fig. 15, which shows the temperature profiles at the end of 4C fast charge for the 15 °C and 0.7 l/min case, where

Table 5: TMS geometry optimisation analysis results: maximum cycle temperature (T_{max}), maximum thermal dispersion among cells on the module (ΔT_{module}) and inside cells (ΔT_{cell}), pressure drop (Δp), hydraulic power (P_h) and necessary auxiliary energy consumption (E_h).

Case	**T_{max} [°C]**		**ΔT_{module} [°C]**		**ΔT_{cell} [°C]**		**Δp [Pa]**		**P_h [W]**		**E_h [Wh]**	
	Geom01	*Geom02*	*Geom01*	*Geom02*	*Geom01*	*Geom02*	*Geom01*	*Geom02*	*Geom01*	*Geom02*	*Geom01*	*Geom02*
15 °C - 0.7 l/min	20.1	18.8	2.0	1.7	2.7	3.7	8.3	11.0	$9.7e^{-5}$	$12.8e^{-5}$	$5.9e^{-5}$	$7.8e^{-5}$
25 °C - 0.7 l/min	29.0	27.9	1.5	1.3	2.0	2.8	7.8	10.1	$9.1e^{-5}$	$11.8e^{-5}$	$5.6e^{-5}$	$7.2e^{-5}$
35 °C - 0.7 l/min	38.4	37.5	1.3	1.1	1.8	2.4	7.4	9.4	$8.7e^{-5}$	$11.0e^{-5}$	$5.3e^{-5}$	$6.7e^{-5}$
25 °C - 4.0 l/min	26.9	26.2	0.4	0.4	3.2	3.6	163.5	147.8	$10.9e^{-3}$	$9.9e^{-3}$	$6.6e^{-3}$	$6.0e^{-3}$

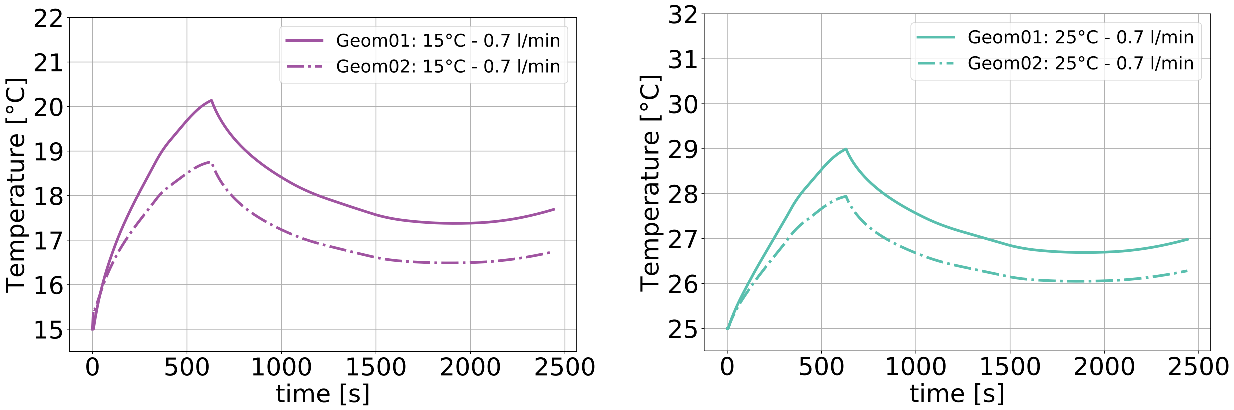

(a) Temperature evolution at 15 °C and 0.7 l/min test.

(b) Temperature evolution at 25 °C and 0.7 l/min test.

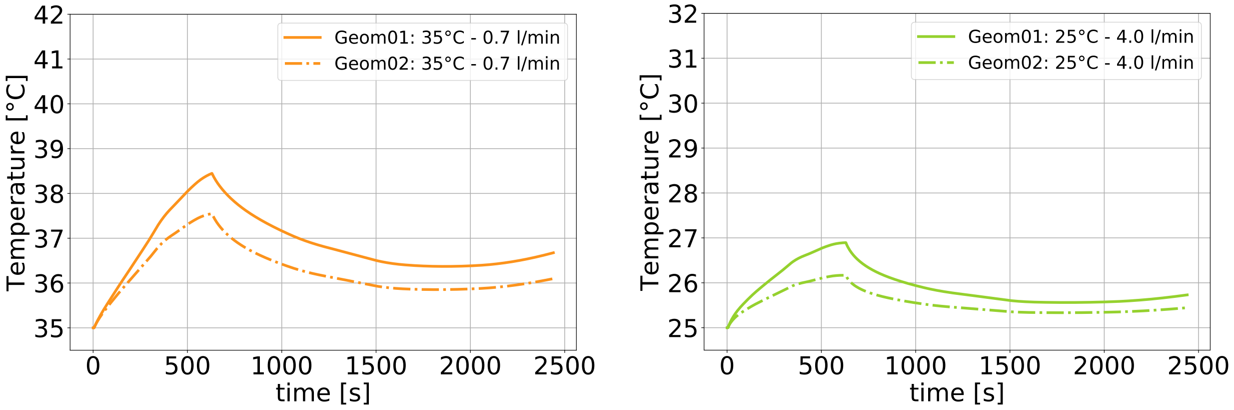

(c) Temperature evolution at 35 °C and 0.7 l/min test.

(d) Temperature evolution at 25 °C and 4.0 l/min test.

Figure 14: Temperature evolution for *Geom01* and *Geom02* on the duct enhancement analysis results.

T_{max} reduction can be seen with the implementation of *Geom02*.

The pressure drop is increased up to 2.7 Pa in *Geom02* due to duct size reduction and fluid velocity rise. Nevertheless, the case with 25 °C and 4.0 l/min shows a different behaviour, as Geom02 has a lower pressure drop than Geom01. This phenomenon can be understood because both curves cross from 2.2 l/min onwards. This means that the increase in pressure loss concerning flow rate in Geom02 is slower than in Geom01. Therefore, Geom02 has an advantage over Geom01 when using higher flow rates.

However, the pressure drop values on the dielectric TMS prototype are low due to the particular viscosity of the employed fluid. This peculiarity results in a reduced necessary pumping energy consumption in comparison with the battery module energy.

Concerning the duct shape change, its volume was reduced by 79.8%, which is especially important for the energy density reduction of the system contrasting with more classical TMS.

Finally, it should be noted that if the dielectric TMS's cycle is operated repeatedly, it is necessary to lower the fluid inlet temperature. By doing this, the cycle-ending temperature would be lowered to at least the ambient temperature, enabling safe repetition of the fast charge.

6. Conclusions

An innovative battery tab- and dielectric-based thermal management system was introduced in this work. Empirical testing was carried out on a functional prototype. Using CFD software, the thermal model of the TMS was also created for the system's thermal simulation and geometry improvement study.

The experimental analysis was made under diverse temperature and volumetric flow rates, repeating the cycle of 4C charge and 1.38C discharge. An exponential temperature-controlling capacity was bounded to the volumetric flow rate, evidencing a thermal jump

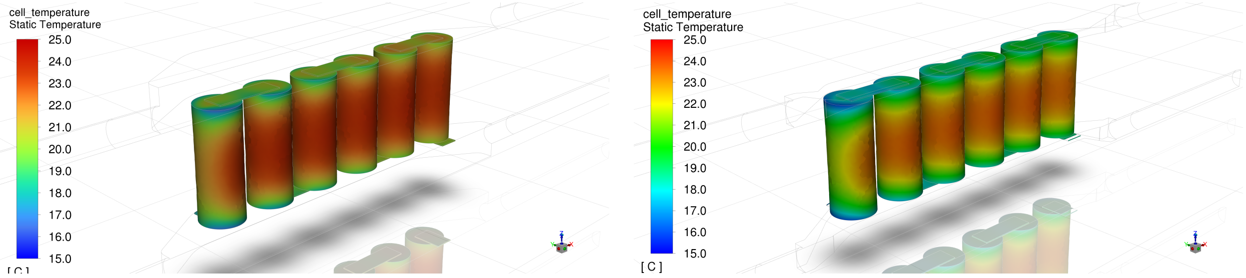

(a) *Geom01* temperature profiles.

(b) *Geom02* temperature profiles.

Figure 15: Comparison of temperature profiles at the end of 4C fast charge with 0.7 l/min flow rate at 15 °C, for *Geom01* and *Geom02*.

reduction of 67% with the lowest flow level activation. Additionally, fluid temperature change influences the heat generation of the cells, reducing at 24.3% the thermal jump when maintaining the cell at least at 25 °C. Moreover, the dielectric TMS proved the potential of preserving the maximum temperature on the battery module, as well as both the thermal gradient among and inside the cells.

A CFD thermal model of the dielectric system was used to study and enhance its heat transfer ability. Modifying dielectric fluid's duct size and shape, thermal management on the system was improved, reducing the operating temperature for all the studied cases. Besides, the temperature difference among cells in the battery module was also reduced with the new geometry by up to 15%. In contrast, the maximum temperature difference inside the cells was increased by as much as 37%. This is a clear effect of the heat transfer capacity increase of the system with the new geometry. Nevertheless, all the temperatures were retained inside the optimal operation span for the batteries.

In terms of auxiliary energy consumption, the low viscosity of the fluid allows for drastically reducing the pumping energy consumption, which was in the worst case, and despite the higher flow rate used, less than 0.004% of the energy exchanged in the battery.

The duct volume decrease of 79.8% attained with the geometry modification is worth noting. This is an illustration of the possibilities of dielectric tab cooling technology. Considering the absence of prototype measuring sensors in a final BM, with the right design, the energy density of a vehicle can be boosted by decreasing the enclosure structure. This, along with the thermal enhancement and reduced auxiliary consumption, exhibits the potential of the proposed dielectric- and tab-based thermal management system.

Acknowledgment

The authors would like to thank the Basque Government and the Basque Agency for Economic Development and Infrastructures for the financial support on the ”CICe2021” (KK 2021/00064) project, as well as all the partners for their support.

References

[1] EIA, Emissions by sector – Greenhouse Gas Emissions from Energy: Overview – Analysis - IEA, 2021. URL: https://www.iea.org/reports/greenhouse-gas-emissions-from-energy-overview/emissions-by-sector.

[2] N. Ash, A. Davies, C. Newton, Renewable electricity requirements to decarbonise transport in Europe with electric vehicles, hydrogen and electrofuels Investigating supply-side constraints to decarbonising the transport sector in the European, Technical Report, Ricardo, 2020.

[3] T. Capuder, D. Miloš Sprčić, D. Zoričić, H. Pandžić, Review of challenges and assessment of electric vehicles integration policy goals: Integrated risk analysis approach, 2020. doi:10.1016/j.ijepes.2020.105894.

[4] M. A. Hannan, M. M. Hoque, A. Mohamed, A. Ayob, Review of energy storage systems for electric vehicle applications: Issues and challenges, Renewable and Sustainable Energy Reviews 69 (2017) 771–789. doi:10.1016/j.rser.2016.11.171.

[5] S. Manzetti, F. Mariasiu, Electric vehicle battery technologies: From present state to future systems, Renewable and Sustainable Energy Reviews 51 (2015) 1004–1012. doi:10.1016/j.rser.2015.07.010.

[6] G. Ning, B. Haran, B. N. Popov, Capacity fade study of lithium-ion batteries cycled at high discharge rates, Journal of Power Sources 117 (2003) 160–169. doi:10.1016/S0378-7753(03)00029-6.

[7] P. Ramadass, B. Haran, R. White, B. N. Popov, Capacity fade of Sony 18650 cells cycled at elevated temperatures: Part II. Capacity fade analysis, Journal of Power Sources 112 (2002) 614–620. doi:10.1016/S0378-7753(02)00473-1.

[8] A. Tomaszewska, Z. Chu, X. Feng, S. O'Kane, X. Liu, J. Chen, C. Ji, E. Endler, R. Li, L. Liu, Y. Li, S. Zheng, S. Vetterlein, M. Gao, J. Du, M. Parkes, M. Ouyang, M. Marinescu, G. Offer, B. Wu, Lithium-ion battery fast charging: A review, eTransportation 1 (2019) 100011. doi:10.1016/j.etran.2019.100011.

[9] J. Shim, R. Kostecki, T. Richardson, X. Song, K. A. Striebel, Electrochemical analysis for cycle performance and capacity

fading of a lithium-ion battery cycled at elevated temperature, Journal of Power Sources 112 (2002) 222–230. doi:10.1016/S0378-7753(02)00363-4.

[10] N. Sato, Thermal behavior analysis of lithium-ion batteries for electric and hybrid vehicles, Journal of Power Sources 99 (2001) 70–77. doi:10.1016/S0378-7753(01)00478-5.

[11] M. Broussely, P. Biensan, F. Bonhomme, P. Blanchard, S. Herreyre, K. Nechev, R. J. Staniewicz, Main aging mechanisms in Li ion batteries, Journal of Power Sources 146 (2005) 90–96. doi:10.1016/j.jpowsour.2005.03.172.

[12] C. K. Huang, J. S. Sakamoto, J. Wolfenstine, S. Surampudi, The Limits of Low-Temperature Performance of Li-Ion Cells, Journal of The Electrochemical Society 147 (2000) 2893. doi:10.1149/1.1393622.

[13] T. Han, B. Khalighi, E. C. Yen, S. Kaushik, Li-ion battery pack thermal management: Liquid versus air cooling, Journal of Thermal Science and Engineering Applications 11 (2019). doi:10.1115/1.4041595.

[14] D. Chen, J. Jiang, G. H. Kim, C. Yang, A. Pesaran, Comparison of different cooling methods for lithium ion battery cells, Applied Thermal Engineering 94 (2016) 846–854. doi:10.1016/j.applthermaleng.2015.10.015.

[15] S. Park, D. Jung, Battery cell arrangement and heat transfer fluid effects on the parasitic power consumption and the cell temperature distribution in a hybrid electric vehicle, Journal of Power Sources 227 (2013) 191–198. doi:10.1016/j.jpowsour.2012.11.039.

[16] W. Zichen, D. Changqing, A comprehensive review on thermal management systems for power lithium-ion batteries, Renewable and Sustainable Energy Reviews 139 (2021) 110685. doi:10.1016/j.rser.2020.110685.

[17] W. Wu, S. Wang, W. Wu, K. Chen, S. Hong, Y. Lai, A critical review of battery thermal performance and liquid based battery thermal management, 2019. doi:10.1016/j.enconman.2018.12.051.

[18] H. Liu, Z. Wei, W. He, J. Zhao, Thermal issues about Li-ion batteries and recent progress in battery thermal management systems: A review, 2017. doi:10.1016/j.enconman.2017.08.016.

[19] Y. Chung, M. S. Kim, Thermal analysis and pack level design of battery thermal management system with liquid cooling for electric vehicles, Energy Conversion and Management 196 (2019) 105–116. doi:10.1016/j.enconman.2019.05.083.

[20] W. Wu, X. Yang, G. Zhang, X. Ke, Z. Wang, W. Situ, X. Li, J. Zhang, An experimental study of thermal management system using copper mesh-enhanced composite phase change materials for power battery pack, Energy 113 (2016) 909–916. doi:10.1016/j.energy.2016.07.119.

[21] M. Mehrabi-Kermani, E. Houshfar, M. Ashjaee, A novel hybrid thermal management for Li-ion batteries using phase change materials embedded in copper foams combined with forced-air convection, International Journal of Thermal Sciences 141 (2019) 47–61. doi:10.1016/j.ijthermalsci.2019.03.026.

[22] S. Wilke, B. Schweitzer, S. Khateeb, S. Al-Hallaj, Preventing thermal runaway propagation in lithium ion battery packs using a phase change composite material: An experimental study, Journal of Power Sources 340 (2017) 51–59. doi:10.1016/j.jpowsour.2016.11.018.

[23] S. A. Hallaj, J. R. Selman, A Novel Thermal Management System for Electric Vehicle Batteries Using Phase-Change Material, Journal of The Electrochemical Society 147 (2000) 3231. doi:10.1149/1.1393888.

[24] X. Duan, G. F. Naterer, Heat transfer in phase change materials for thermal management of electric vehicle battery modules, International Journal of Heat and Mass Transfer 53 (2010) 5176–5182. doi:10.1016/j.ijheatmasstransfer.2010.07.044.

[25] M. Suresh Patil, J. H. Seo, M. Y. Lee, A novel dielectric fluid immersion cooling technology for Li-ion battery thermal management, Energy Conversion and Management 229 (2021). doi:10.1016/j.enconman.2020.113715.

[26] K. V. Jithin, P. K. Rajesh, Numerical analysis of single-phase liquid immersion cooling for lithium-ion battery thermal management using different dielectric fluids, International Journal of Heat and Mass Transfer 188 (2022) 122608. doi:10.1016/j.ijheatmasstransfer.2022.122608.

[27] Y. F. Wang, J. T. Wu, Thermal performance predictions for an HFE-7000 direct flow boiling cooled battery thermal management system for electric vehicles, Energy Conversion and Management 207 (2020). doi:10.1016/j.enconman.2020.112569.

[28] P. Dubey, G. Pulugundla, A. K. Srouji, Direct comparison of immersion and cold-plate based cooling for automotive li-ion battery modules, Energies 14 (2021). doi:10.3390/en14051259.

[29] M. Al-Zareer, I. Dincer, M. A. Rosen, Electrochemical modeling and performance evaluation of a new ammonia-based battery thermal management system for electric and hybrid electric vehicles, Electrochimica Acta 247 (2017) 171–182. doi:10.1016/j.electacta.2017.06.162.

[30] T. Ahmad, A. Mishra, S. Ghosh, C. S. Casari, Identifying Efficient Cooling Approach of Cylindrical Lithium-Ion Batteries, Energy Technology 10 (2022). doi:10.1002/ente.202100888.

[31] I. A. Hunt, Y. Zhao, Y. Patel, J. Offer, Surface Cooling Causes Accelerated Degradation Compared to Tab Cooling for Lithium-Ion Pouch Cells, Journal of The Electrochemical Society 163 (2016) A1846–A1852. doi:10.1149/2.0361609jes.

[32] O. Dondelewski, T. Szemberg O'Connor, Y. Zhao, I. A. Hunt, A. Holland, A. Hales, G. J. Offer, Y. Patel, The role of cell geometry when selecting tab or surface cooling to minimise cell degradation, eTransportation 5 (2020). doi:10.1016/j.etran.2020.100073.

[33] D. Dubey, A. Mishra, S. Ghosh, M. V. Reddy, R. Pandey, Geometry-influenced cooling performance of lithium-ion battery, Applied Thermal Engineering 230 (2023). URL: https://doi.org/10.1016/j.applthermaleng.2023.120723. doi:10.1016/j.applthermaleng.2023.120723.

[34] S. Li, N. Kirkaldy, C. Zhang, K. Gopalakrishnan, T. Amietszajew, L. B. Diaz, J. V. Barreras, M. Shams, X. Hua, Y. Patel, G. J. Offer, M. Marinescu, Optimal cell tab design and cooling strategy for cylindrical lithium-ion batteries, Journal of Power Sources 492 (2021) 229594. doi:10.1016/j.jpowsour.2021.229594.

[35] T. G. Tranter, R. Timms, P. R. Shearing, D. J. L. Brett, Communication—Prediction of Thermal Issues for Larger Format 4680 Cylindrical Cells and Their Mitigation with Enhanced Current Collection, Journal of The Electrochemical Society 167 (2020) 160544. doi:10.1149/1945-7111/abd44f.

[36] Lithium-ion 26650 Cells — Nanophosphate Batteries — Lithium Werks, ???? URL: https://lithiumwerks.com/products/lithium-ion-26650-cells/.

[37] E. Gonzalez-Aguirre, J. Gastelurrutia, M. S. Patil, L. del Portillo-Valdes, Avoiding Thermal Issues During Fast Charging Starting with Proper Cell Selection Criteria, Journal of The Electrochemical Society 168 (2021) 110523. doi:10.1149/1945-7111/ac3348.

[38] E. Gonzalez-Aguirre, I. Aranburu, J. Gastelurrutia, L. Diaz, M. S. Patil, L. del Portillo-Valdes, 1D Dynamic Thermal Model

Development for a Battery Hybrid Thermal Management System, in: 2021 IEEE Vehicle Power and Propulsion Conference (VPPC), IEEE, 2021, pp. 1–6. URL: https://ieeexplore.ieee.org/document/9699281/. doi:10.1109/VPPC53923.2021.9699281.

[39] 3M, 3M HFE 7200, 2009. URL: https://multimedia.3m.com/mws/media/199819O/3m-novec-7200-engineered-fluid-en.pdf.

[40] 3M, 3M ™ Thermal Management Fluids, 2008. URL: https://multimedia.3m.com/mws/media/569860O/3mtm-thermal-management-fluids-for-military-aerospace-apps.pdf.

[41] Y. Zheng, H. Gao, Q. Chen, X. Meng, J. Wu, Isobaric heat capacity measurements of liquid HFE-7200 and HFE-7500 from 245 to 353K at pressures up to 15MPa, Fluid Phase Equilibria 372 (2014) 56–62. doi:10.1016/j.fluid.2014.03.017.

[42] P. Warrier, A. S. Teja, Density, viscosity, and thermal conductivity of mixtures of 1-ethoxy-1,1,2,2,3,3,4,4,4-nonafluorobutane (HFE 7200) with methanol and 1-ethoxybutane, Journal of Chemical and Engineering Data 56 (2011) 4291–4294. doi:10.1021/je1011828.

[43] D. Bernardi, E. Pawlikowski, J. Newman, A General Energy Balance for Battery Systems, Journal of the Electrochemical Society 132 (1985) 5–12. doi:10.1149/1.2113792.

[44] H. G. Schweiger, O. Obeidi, O. Komesker, A. Raschke, M. Schiemann, C. Zehner, M. Gehnen, M. Keller, P. Birke, Comparison of several methods for determining the internal resistance of lithium ion cells, Sensors 10 (2010) 5604–5625. doi:10.3390/s100605604.

[45] K. E. Thomas, C. Bogatu, J. Newman, Measurement of the Entropy of Reaction as a Function of State of Charge in Doped and Undoped Lithium Manganese Oxide, Journal of The Electrochemical Society 148 (2001) A570. doi:10.1149/1.1369365.

[46] ISO, ISO 22007-2: Plastics — Determination of thermal conductivity and thermal diffusivity — Part 2: Transient plane heat source (hot disc) method, Annual Book ofASTM Standards 2008 (2008) 17.

[47] H. Maleki, S. A. Hallaj, J. R. Selman, R. B. Dinwiddie, H. Wang, Thermal Properties of Lithium-Ion Battery and Components, Journal of The Electrochemical Society 146 (1999) 947–954. doi:10.1149/1.1391704.

[48] J. Gastelurrutia, J. C. Ramos, G. S. Larraona, A. Rivas, J. Izagirre, L. Del Río, Numerical modelling of natural convection of oil inside distribution transformers, Applied Thermal Engineering 31 (2011) 493–505. doi:10.1016/j.applthermaleng.2010.10.004.

[49] T. H. Shih, W. W. Liou, A. Shabbir, Z. Yang, J. Zhu, A new k-eddy viscosity model for high reynolds number turbulent flows, Computers and Fluids 24 (1995) 227–238. doi:10.1016/0045-7930(94)00032-T.

[50] H. C. Chen, V. C. Patel, Near-wall turbulence models for complex flows including separation, AIAA Journal 26 (1988) 641–648. doi:10.2514/3.9948.

[51] P. J. Boache, Perspective: A method for uniform reporting of grid refinement studies, Journal of Fluids Engineering, Transactions of the ASME 116 (1994) 405–413. doi:10.1115/1.2910291.